

Simulation of electron energy loss spectra of nanomaterials with linear-scaling density functional theory

This content has been downloaded from IOPscience. Please scroll down to see the full text.

2016 J. Phys.: Condens. Matter 28 195202

(<http://iopscience.iop.org/0953-8984/28/19/195202>)

View [the table of contents for this issue](#), or go to the [journal homepage](#) for more

Download details:

IP Address: 131.111.184.102

This content was downloaded on 21/08/2017 at 10:36

Please note that [terms and conditions apply](#).

You may also be interested in:

[Linear-scaling density functional theory using the projector augmented wave method](#)

Nicholas D M Hine

[Linear-scaling density functional theory simulations of polar semiconductor nanorods](#)

Nicholas D M Hine, Philip W Avraam, Paul Tangney et al.

[Applications of large-scale density functional theory in biology](#)

Daniel J Cole and Nicholas D M Hine

[Core-level spectroscopy calculation and the plane wave pseudopotential method](#)

Shang-Peng Gao, Chris J Pickard, Alexander Perlov et al.

[O\(N\) methods in electronic structure calculations](#)

D R Bowler and T Miyazaki

[Using ONETEP for accurate and efficient O\(N\) density functional calculations](#)

Chris-Kriton Skylaris, Peter D Haynes, Arash A Mostofi et al.

[Robust theoretical modelling of core ionisation edges for quantitative electron energy loss spectroscopy of B- and N-doped graphene](#)

T P Hardcastle, C R Seabourne, D M Kepaptsoglou et al.

[Recent progress in linear-scaling density functional calculations with plane waves and pseudopotentials: the ONETEP code](#)

Chris-Kriton Skylaris, Peter D Haynes, Arash A Mostofi et al.

Simulation of electron energy loss spectra of nanomaterials with linear-scaling density functional theory

E W Tait¹, L E Ratcliff², M C Payne¹, P D Haynes³ and N D M Hine⁴

¹ Theory of Condensed Matter Group, Cavendish Laboratory, 19 J J Thomson Avenue, Cambridge, CB3 0HE, UK

² Leadership Computing Facility, Argonne National Laboratory, 9700 South Cass Avenue, Building 240, Argonne, IL 60439, USA

³ Department of Materials, Imperial College London, Exhibition Road, London, SW7 2AZ, UK

⁴ Theory Group, Department of Physics, University of Warwick, Coventry, CV4 7AL, UK

E-mail: ewt23@cam.ac.uk

Received 12 February 2016, revised 16 March 2016

Accepted for publication 24 March 2016

Published 20 April 2016



CrossMark

Abstract

Experimental techniques for electron energy loss spectroscopy (EELS) combine high energy resolution with high spatial resolution. They are therefore powerful tools for investigating the local electronic structure of complex systems such as nanostructures, interfaces and even individual defects. Interpretation of experimental electron energy loss spectra is often challenging and can require theoretical modelling of candidate structures, which themselves may be large and complex, beyond the capabilities of traditional cubic-scaling density functional theory. In this work, we present functionality to compute electron energy loss spectra within the ONETEP linear-scaling density functional theory code. We first demonstrate that simulated spectra agree with those computed using conventional plane wave pseudopotential methods to a high degree of precision. The ability of ONETEP to tackle large problems is then exploited to investigate convergence of spectra with respect to supercell size. Finally, we apply the novel functionality to a study of the electron energy loss spectra of defects on the (1 0 1) surface of an anatase slab and determine concentrations of defects which might be experimentally detectable.

Keywords: EELS, ELNES, linear scaling, defects, titanium dioxide, theoretical spectroscopy, electron energy loss spectroscopy

(Some figures may appear in colour only in the online journal)

1. Introduction

Continual improvements in microscope technology in recent years have greatly increased the utility of electron energy loss spectroscopy (EELS) in the characterization of materials. Near atomic resolution is now routinely achieved, and element mapping in samples is frequently undertaken. As well as positional information on dopants and impurities, information about the

local chemical environment [1, 2] of an atom may be obtained, including oxidation state [3, 4] and coordination of individual atoms [5]. Signatures from surfaces may also be extracted [6].

Greater information about the local structure and chemistry is encoded in the energy loss near edge structure (ELNES), but interpretation of this is hampered by a lack of simple methods to extract this information from spectra. Theoretical spectroscopy can be invaluable in such cases as it provides a means to compute spectra for proposed model structures, from which the best match to experiment can be found [7].

While theoretical spectroscopy is promising for analyzing experimental spectra, applying it to large systems has proven

 Original content from this work may be used under the terms of the [Creative Commons Attribution 3.0 licence](https://creativecommons.org/licenses/by/3.0/). Any further distribution of this work must maintain attribution to the author(s) and the title of the work, journal citation and DOI.

challenging, due to the poor scaling of traditional density functional theory methods with system size. This is especially frustrating as many technologically and scientifically interesting systems can only be modelled using hundreds to thousands of atoms—examples include whole nanoparticles, grain boundaries, well-converged isolated defects, and thin film surfaces.

In this work, we propose a means to overcome this system-size barrier by implementing functionality for EELS simulation within the framework of a code suitable for very large-scale calculations, ONETEP [8]. Total energy and force calculations are available in ONETEP with linear-scaling computational effort, due to a combination of methods based on optimisation of a representation of the single electron density matrix using a highly-efficient set of *in situ* optimized local orbitals and sparse matrix techniques making use of a hybrid OpenMP-MPI parallel strategy [9]. While our proposed method for EELS simulations requires a one-off $\mathcal{O}(N^3)$ diagonalization to obtain Kohn–Sham eigenstates, the minimal basis set means computational costs are reasonable for systems up to around three to four thousand atoms.

2. Methods

Simulation of EELS using density functional theory is most commonly achieved using Fermi’s Golden Rule to obtain the imaginary part of the dielectric function in terms of dipole matrix elements between core and conduction band states. In atomic units, this gives:

$$\epsilon_2(\omega) = \frac{1}{\Omega} \sum_c \sum_i |\langle \psi_i | \exp(i\mathbf{q} \cdot \mathbf{r}) | \psi_c \rangle|^2 \delta(E_i - E_c - \omega)$$

where ω is the transition energy, Ω is the volume of the unit cell, ψ_i are (all-electron) conduction band states, ψ_c is a core state, with respective energies E_i and E_c . \mathbf{r} is a position operator defined as the displacement from the nucleus whose core electrons are being excited, and \mathbf{q} is the momentum transfer. The δ -function conserves energy and can be replaced with a Gaussian to introduce appropriate broadening.

In the dipole approximation this expression becomes:

$$\epsilon_2(\omega) = \frac{1}{\Omega} \sum_c \sum_i |\mathbf{q} \cdot \langle \psi_i | \mathbf{r} | \psi_c \rangle|^2 \delta(E_i - E_c - \omega) \quad (1)$$

where we have expanded the complex exponential to first order, noting that the orthogonality of wavefunctions removes the constant term in the Maclaurin series. This form is especially useful as the momentum transfer can be supplied during post-processing (see section 2.4) and thus many different (small) momentum transfers can be investigated using the results of a single DFT calculation.

The ONETEP code implements a linear scaling density functional theory [10, 11] (LS-DFT) scheme based on the density matrix formalism [8]. The density matrix is represented in terms of a set of localized basis functions [12] referred to as nonorthogonal generalized Wannier functions—NGWFs [13], ϕ_α , and a density kernel $K^{\alpha\beta}$:

$$\rho(\mathbf{r}, \mathbf{r}') = \sum_{\alpha, \beta} K^{\alpha\beta} \phi_\alpha(\mathbf{r}) \phi_\beta(\mathbf{r}') \quad (2)$$

It is known that materials with a band gap exhibit ‘near-sightedness’ [14]: their density matrix decays exponentially with $|\mathbf{r} - \mathbf{r}'|$. It is therefore possible to impose a range-based truncation on the density kernel so that it becomes a sparse matrix [15].

The NGWFs are expressed in terms of an underlying basis of periodic sinc (psinc) functions, which have been shown to be equivalent to a plane-wave basis [16]. The NGWFs are strictly localized within a sphere of a chosen cutoff radius centred on the atom to which they are attached. The ONETEP code uses a nested loop optimisation method: in the outer loop, NGWFs are optimized using a conjugate gradient algorithm to minimize the total energy; for each outer loop step, the density kernel is optimized to minimize the energy for the current NGWFs subject to the conditions that the density matrix remains idempotent and electron number is conserved.

The underlying psinc basis permits use of fast Fourier transforms (FFTs) to obtain reciprocal space representations, such as for nonlocal projectors and for the kinetic energy operator. To increase the efficiency of FFTs in large systems, we make use of structures called FFT Boxes. These are small subspaces of the simulation cell, centred on a given NGWF and large enough to completely contain all NGWFs which overlap with it [13].

2.1. Conduction optimisation

The nested loop optimisation method produces a kernel and NGWF set which are optimized to represent the valence manifold accurately and efficiently. However, these NGWFs often represent unoccupied conduction states rather poorly. To obtain an accurate representation of the low-lying conduction band states, we follow the procedure described in Ratcliff *et al* and introduce a second kernel and a second set of NGWFs: $\chi_\alpha(\mathbf{r})$. These conduction NGWFs are optimized to represent the low-lying conduction states [17]. They can be combined with the valence NGWFs to produce a joint representation in which all valence and conduction eigenstates can be accurately represented.

2.2. Projector augmented wave

In ONETEP the projector augmented wave (PAW) formalism of Blöchl can be used [18, 19] to recover all-electron results from calculations including only valence electrons explicitly. PAW enables calculations with a much smaller plane-wave basis (or, equivalently, a smaller underlying psinc basis) than would be required for either an all-electron or norm-conserving pseudopotential approach.

All-electron matrix elements of the dipole operator between conduction band eigenstates and core states are required for simulated EELS. In PAW these take the form [20]

$$\langle \psi_i | \mathbf{r} | \psi_c \rangle = \langle \tilde{\psi}_i | \mathbf{r} | \psi_c \rangle + \sum_\nu \langle \tilde{\psi}_i | \tilde{p}_\nu \rangle (\langle \varphi_\nu | \mathbf{r} | \psi_c \rangle - \langle \tilde{\varphi}_\nu | \mathbf{r} | \psi_c \rangle) \quad (3)$$

Here ψ_i is an all-electron conduction band wavefunction, $\tilde{\psi}_i$ is the corresponding pseudowavefunction, ψ_c is a core wavefunction associated with a particular atom, \tilde{p}_ν is a projector and $\tilde{\varphi}_\nu$ and φ_ν are pseudo and all-electron partial waves respectively.

2.3. Implementation of EELS simulation

In a post-processing step after a converged calculation, the Kohn–Sham Hamiltonian matrix expressed in the NGWF representation is diagonalized to obtain the Kohn–Sham (pseudo-) wavefunctions $\tilde{\psi}_i$ in terms of NGWF coefficients $(M^\dagger)_i^\alpha$:

$$\langle \tilde{\psi}_i | = (M^\dagger)_i^\alpha \langle \phi_\alpha | \quad (4)$$

The calculation of matrix elements then proceeds according to (3), via three steps:

- (i) Matrix elements are computed on the Cartesian grid between NGWFs and the core state $\langle \phi_\alpha | \mathbf{r} | \psi_c \rangle$, and between NGWFs and projectors, $\langle \phi_\alpha | \tilde{p}_\nu \rangle$.
- (ii) The PAW correction term is calculated, taking the form $\sum_\nu \langle \phi_\alpha | \tilde{p}_\nu \rangle (\langle \varphi_\nu | \mathbf{r} | \psi_c \rangle - \langle \tilde{\varphi}_\nu | \mathbf{r} | \psi_c \rangle)$, calculating the partial wave terms on a logarithmic radial grid to ensure high accuracy.
- (iii) The above two terms are combined and the result is multiplied by the NGWF wavefunction coefficient matrix to produce matrix elements between all-electron conduction wavefunctions and core wavefunctions.

The first step requires the generation of kets of the form $r_x | \psi_c \rangle$ on a regular real space grid. Note that the PAW formalism means that it is not necessary to accurately reproduce the part of the core orbital which lives within the PAW sphere on the regular grid: the radial grid terms will account for that part of the matrix element. This means that the method remains suitable even for tightly-confined core orbitals of higher- Z elements, for which the PAW radial grid terms account for almost all of the matrix element. For first-row and second-row elements, however, the confinement even of the $1s$ orbitals is not so tight, and the first term in (3) must be reproduced accurately.

The most straightforward approach to generating $r_x | \psi_c \rangle$ would be to transform the core orbitals directly to the real space grid in an FFT box centered on the atom, and multiply by the position operator before integrating the product of this function and the NGWF. However, it was determined that due to the high spatial frequencies of core orbitals, this approach is not sufficiently accurate on a Cartesian grid of feasible spacing.

Instead, we use a Fourier space method for applying the position operator:

$$\sum_{\mathbf{G}}^{\mathbf{G}_{\max}} (\nabla_{\mathbf{G}} \psi_c(\mathbf{G})) \exp(i\mathbf{G} \cdot \mathbf{r}) = -i\mathbf{r} \psi_c(\mathbf{r}) \quad (5)$$

This approach gives considerably higher accuracy in reproduction of the core orbitals since it calculates directly the Fourier transform of the product $\mathbf{r} \psi_c(\mathbf{r})$

Note that the diagonalisation of the Hamiltonian in the basis of NGWFs introduces a cost of $\mathcal{O}(N^3)$ to an EELS calculation. This diagonalisation is, however, a one-off calculation per system and its cost will only become significant compared to the cost of NGWF optimisation for very large systems, well over the 2000–4000 atom systems we aim to target with this methodology.

2.4. Calculation of spectra

Using (3) provides matrix elements which can be combined with (1) to provide spectra, subject to appropriate broadening via convolution with a suitable function. This is usually a Gaussian and/or a Lorentzian, whose widths are usually chosen so as to approximately match the broadening in a corresponding experiment, due to lifetime and instrumental effects. For this operation we rely on the OPTADoS code [21]. This code supports a number of different broadening schemes: here we will use fixed broadening in most cases, with energy-dependent lifetime broadening in selected cases, as indicated in the figure captions. The OPTADoS code also accepts a momentum transfer parameter, a unit vector in the direction of the momentum transfer. For our simulated spectra an isotropic average over directions was taken.

In the prediction of spectra for solids, it is often necessary to use a high density of k -points for Brillouin zone integration to achieve a well-converged spectrum. In linear-scaling DFT approaches it is more common simply to use a larger supercell with periodic replicas of the primitive cell, which produces an effective k -point sampling equal to the number of repeats of the primitive cell in each direction.

2.5. Core holes

The simulation of the electron energy loss process using Fermi's Golden Rule within KS-DFT neglects the interaction between the excited electron-hole pair. A reasonable approximation which is widely used to improve this is to introduce a core hole, i.e. a missing electron in the appropriate core level of the atom whose spectrum is required. Within pseudopotential and PAW methods, this is achieved by assigning this atom a modified pseudopotential, which takes into account the vacant core orbital. Several methods exist for this: the simplest is to use a pseudopotential for an atom with an atomic number one greater than the actual species (the 'Z+1' method). Greater accuracy can be obtained by regenerating the appropriate PAW data set with fixed occupancies corresponding to the promotion of an electron from the core level to the lowest previously-unoccupied state. For example, for a core hole in the $1s$ orbital of a carbon atom, the configuration solved for would be $1s^1 2s^2 2p^3$. The method, while somewhat empirical in nature, has been widely shown to significantly improve agreement of predicted spectra with experimental results. However, it comes with the disadvantage that calculations must be repeated for each atom for which predicted EEL spectra are required.

2.6. Absolute energy offset

In many applications, the ability to predict changes in the spectrum for a particular element in different local environments is of more significance than to predict the absolute energy of the spectrum. Nevertheless, manual alignment of the offset of the edge by comparison to experiment is clearly undesirable. Mizoguchi *et al* [22] proposed a method to compute absolute offsets in the context of pseudopotential methods by comparison of the energies of valence pseudopotential and all-electron calculations for ground-state and excited-state atoms. In this approach, one computes three excitation energies: (i) the difference in total energy of the full system between the ground state and a state with the core hole potential present and an extra electron placed in the lowest energy conduction state; (ii) the change in total energy of the isolated all-electron atom under a similar promotion of an electron from the core orbital to the lowest unoccupied state; and (iii) the difference in total energy between the isolated ground state pseudo-atom and the core hole potential with a promoted electron. Essentially, one is taking the excitation energy in the context of the real system, subtracting off the response of the pseudised atom, and adding back on the response of the all-electron atom, in an attempt to take into account the response of the all-electron atom in the real environment.

$$\begin{aligned}
 E_{\text{edge}} = & (E_{\text{sys}+\text{ch}+\text{e}} - E_{\text{sys,gs}}) \\
 & + (E_{\text{aeatom}+\text{ch}+\text{e}} - E_{\text{aeatom,gs}}) \\
 & - (E_{\text{psatom}+\text{ch}+\text{e}} - E_{\text{psatom,gs}}) \quad (6)
 \end{aligned}$$

Where $E_{\text{sys}+\text{ch}+\text{e}}$ is the total energy of the system as calculated with a core hole potential and an electron in the lowest state of the conduction band. $E_{\text{sys,gs}}$ is the ground state energy of the system (no core hole, no electron in the conduction band). $E_{\text{aeatom}+\text{ch}+\text{e}}$ and $E_{\text{aeatom,gs}}$ are the all electron total energies of the isolated atom under consideration with the core hole (and excited electron) and in the ground state respectively. Finally $E_{\text{psatom}+\text{ch}+\text{e}}$ and $E_{\text{psatom,gs}}$ are the pseudoatom total energies of the isolated atom under consideration with the core hole (and excited electron) and in the ground state respectively.

One then uses this excitation energy as the offset of the lowest energy state in the conduction band. Whilst there is not perfect agreement with experimental edge onset energies, values computed using (6) are correct to approximately 1–2%, and the method has met with widespread success in predicting chemical shifts for a given element between different materials [28–31].

3. Demonstration of methodology

Our first task is to demonstrate that the implementation of simulated electron energy loss spectroscopy, within the context of linear-scaling DFT with local orbitals, is capable of generating results systematically equivalent to widely used simulated EELS methodology. We first compare the output of the current implementation to plane-wave pseudopotential (PWP) methods, utilising the widely-used PWP package,

Table 1. Details of supercells used for simulation of a range of crystalline solids.

Material	Atoms	a,b,c/Å	Space group	Reference
Graphite	200	12.32, 12.32, 13.42	P6 ₃ /mmc	[23]
Diamond	216	10.60, 10.60, 10.60	Fd $\bar{3}$ m	[24]
Silicon	216	16.29, 16.29, 16.29	Fd $\bar{3}$ m	[25]
MgO	216	12.64, 12.64, 12.64	Fm $\bar{3}$ m	[26]

Note: Structures were obtained via the inorganic crystal structure database [27].

CASTEP [32] (Version 8.0). The academic release of ONETEP was used (Version 4.3.3.4).

We have chosen a range of simple systems to span wide- and narrow-band-gap materials. In each case we generate an equivalent supercell within ONETEP and CASTEP, resulting in the set of systems shown in table 1. For the purposes of sections 3.1 and 3.2 we are primarily interested in the capacity of our implementation to produce predicted spectra for a given input geometry which match closely those produced by other methods. For this reason the simulation cells used were not subject to relaxation of the lattice constant. In the interests of consistency the experimental value of the lattice constants are used throughout.

For this preliminary investigation no core holes were used. ONETEP and CASTEP calculations were performed at a kinetic energy cut-off of 800 eV, which is well-converged for all materials studied here. We utilize the PBE functional [33], which as is widely-understood, would be expected to underestimate band-gaps but otherwise produce geometry and electronic structure in good agreement with experiment. Only the Γ point is sampled for the supercell ground state calculations. For the ONETEP calculations, we use the PAW data sets of Jollet, Torrent and Holzwarth [34]. For CASTEP the *on the fly* pseudopotential generator was used. Both sets have been shown to be highly accurate through comparisons made as part of the ‘Delta’ project [35].

Valence and conduction NGWFs were truncated in ONETEP to a radius of 10.0 a_0 (5.3 Å) for all materials, which we verified was able to produce well-converged densities of states for all systems in the valence and conduction bands. Kernel truncation was not applied in these systems as they are too small for this to be worthwhile.

The all-electron calculations were performed using the ELK code [36]. The parameter `rgkmax`, which controls basis set size, was set to 7. Muffin tin radii for the species simulated were (Å): carbon: 0.95 oxygen: 0.95 magnesium: 1.16. An LDA functional was used. Core hole effects were included using a ‘Z + 1’ approximation as described in the ELK documentation.

3.1. Comparison to plane-wave methods

As the underlying basis of psinc functions used to express the local orbitals in a ONETEP calculation is equivalent to plane waves, we expect a very high degree of agreement between predicted spectra and those produced using a plane wave

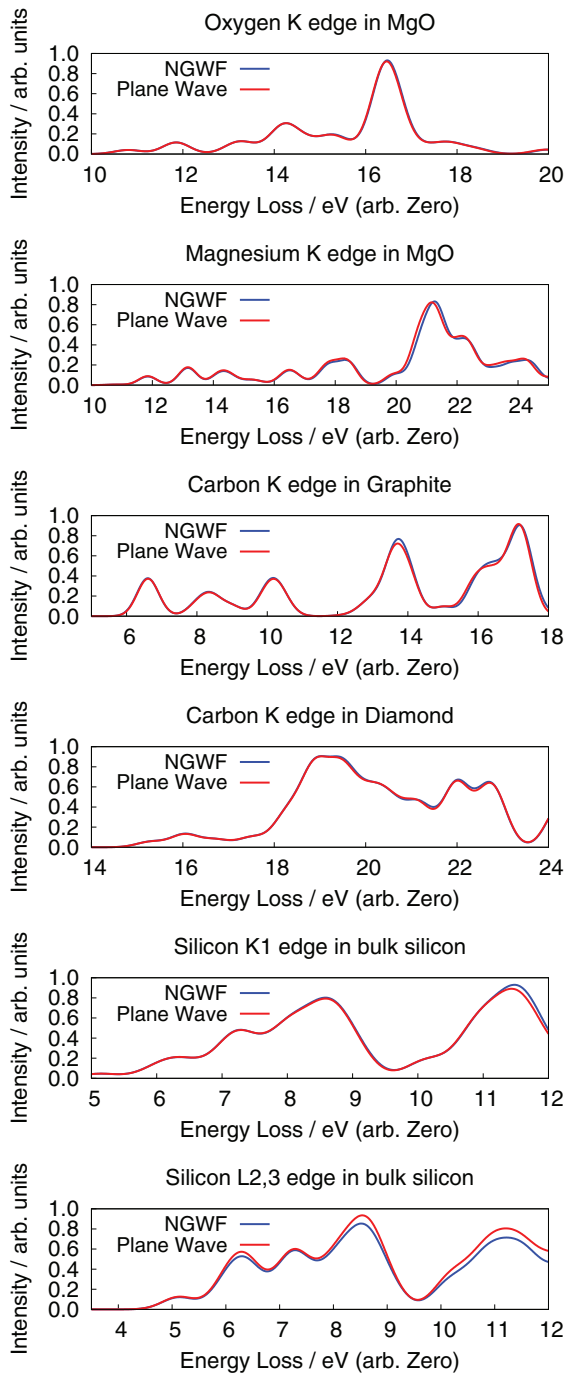


Figure 1. Comparison of predicted spectra generated with the new methodology in ONETEP with plane wave results, for each of the materials listed in table 1. Spectra have been manually aligned such that the first peaks of the plane wave and NGWF spectra coincide.

code. This is seen in the case of the tested systems, as long as the low energy conduction states can be well converged. Using a low smearing to compute spectra (far lower than the broadening usually observed in experiment) permits detailed comparison of fine structure between the two simulation methods. We do not calculate absolute energy offsets at this stage, but rather align the energy axis to the first peak of the spectrum, to aid detailed comparison of the shape of the predicted spectrum. Note that we will not perform any rescaling

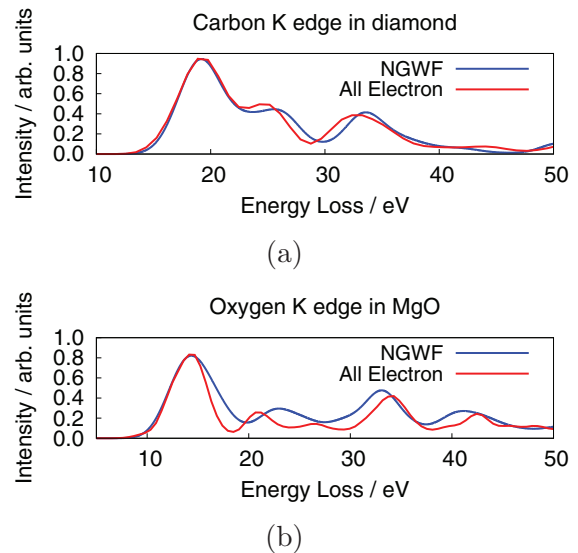


Figure 2. Detailed comparison between ONETEP and all-electron predicted spectra for diamond (a) and oxygen in magnesium oxide (b). Spectra have been manually aligned using the first peak of the spectrum.

for this comparison, providing a powerful test of how robust our method is across different PAW data sets.

Figure 1 shows this comparison in the case of magnesium oxide, graphite, diamond and silicon. In all cases we see almost perfect agreement in terms of relative peak position, peak height, and relative peak heights for at least the first 10 eV above the onset. Beyond this, the quality of the representation of the conduction band states in ONETEP is somewhat reduced, and there are minor discrepancies in peak heights, though these would not impair qualitative comparisons.

3.2. Comparison to all-electron methods

Simulations of the diamond and magnesium oxide systems were undertaken using the all-electron ELK code to provide a further point of comparison for our method. Given the computationally demanding nature of all-electron calculations, smaller supercells were used. The diamond simulation was conducted in a $2 \times 2 \times 2$ supercell and the magnesium oxide simulation in an unreduced eight atom unit cell. Monkhorst-Pack k -point meshes of $10 \times 10 \times 10$ and $8 \times 8 \times 8$ respectively were used.

Figure 2 shows a comparison between ONETEP results with one core hole and broadened with a 1.5 eV width Gaussian and all-electron results. Once again, we see a very good agreement, validating the PAW methodology in general and our Fourier space method for displacement core kets ($r_x|\psi_c\rangle$) in particular. It should further be noted that the ELK does not use the dipole approximation and the close agreement of our results validates the use of (1) in this work. Note also that even though conduction NGWFs in the ONETEP calculation have only been optimised for the first roughly 10–20 eV beyond the conduction band edge, there is nevertheless relatively good agreement with all-electron methods over the whole range of 10–50 eV.

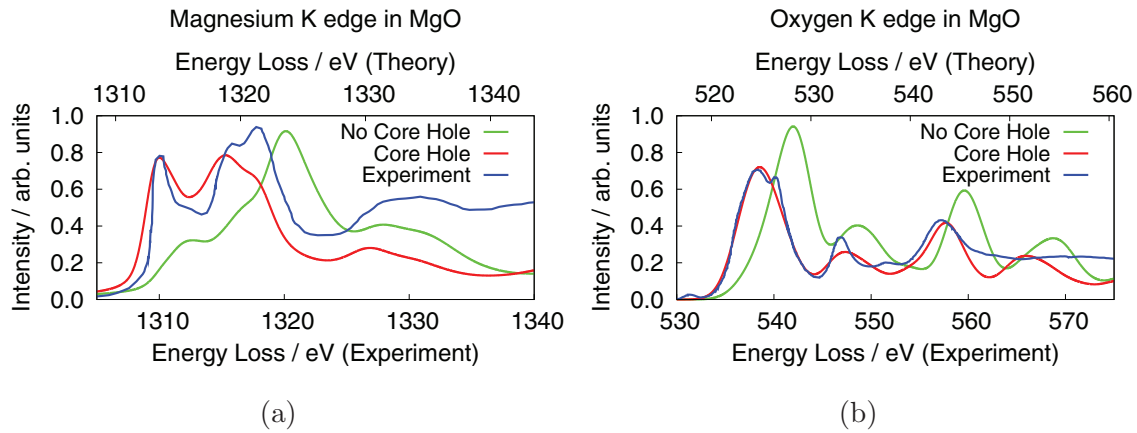


Figure 3. Detailed comparison between ONETEP and experimental spectra for Mg (a) and O (b) K-edges in MgO showing the effect of including a full core hole on the computed spectrum. Upper energy axis for simulated spectra. Lower energy axis experimental spectra. In the case of the magnesium K edge a lifetime broadening scheme was used. Experimental data reproduced from [37] with permission.

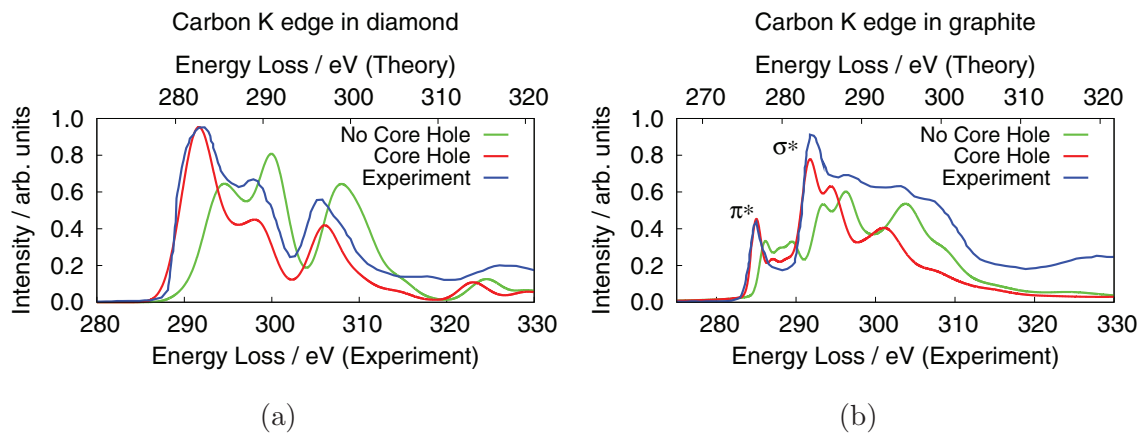


Figure 4. Comparison of predicted spectra from the current method with experimental spectra for carbon K-edges in diamond (a) and graphite (b). The inclusion of a core hole dramatically improves the agreement of the predicted diamond spectrum with experiment. Graphite, however, has greater screening and less of a change is seen. Upper energy axis for simulated spectra. Lower energy axis experimental spectra. A lifetime broadening scheme was used for the carbon K edge in graphite. Experimental data reproduced from [38] with permission.

3.3. Comparison to experimental spectra

Having established that the methodology is in excellent agreement with existing state-of-the-art techniques for electron energy loss spectroscopy based on KS-DFT, we are now in a position to compare directly with experimental spectra. For this comparison we will show that it becomes considerably more important to include the effects of core holes, so we show results both with and without a core hole included for a chosen atom. Note that the excellent agreement between the current methodology and the well-tested plane-wave pseudo-potential formalism, shown in figure 1, can be shown to be retained fully when using a PAW dataset with a core hole included.

The experimental spectra we reproduce from the literature [37, 38] were obtained using transmission electron microscopy at a variety of facilities: see the individual references for more detail. Our simulated spectra are computed under the assumption of zero momentum transfer. To facilitate comparison to experimental results we apply a 1.5 eV Gaussian broadening, which roughly matches the effective

resolution of older spectra (though current state-of-the-art facilities can improve upon this resolution). In the case of graphite and the magnesium K edge in MgO, lifetime broadening effects were also included, since it is clear that there is increasing broadening at higher energies. In all cases, since both experimental and computed spectra are measured in arbitrary units, we rescale the experimental results vertically for ease of comparison, based on best agreement of the first peak or the first and second peaks. A test of simulated spectra for the carbon K edge in diamond and the oxygen K edge in MgO indicated that there is a minimal difference between spectra computed using relaxed instead of unrelaxed lattices once a physically reasonable broadening has been applied.

Our simulated spectra have been offset by an energy shift which places the lowest conduction band state at the energy computed using the Mizoguchi method described in section 2.6. The same offset was applied to spectra simulated with and without core holes (for a given system). This offset method has been used in all our simulated spectra other than those shown in figures 1 and 2.

Figure 3 shows results for Mg and O K-edges in bulk crystalline magnesium oxide. Comparing the spectra without a core hole (green) and experimental (blue) lines, we see initially a poor agreement between computed and experimental spectra. Given the large band gap of the material it is likely that the core hole potential is rather weakly screened. Thus a core hole potential must be included to reproduce the experimental spectrum (red line, see next section for further discussion).

In the case of carbon-based materials, diamond and graphite, figure 4 shows that there is already a quite impressive similarity between experimental results and simulation even without core holes. Relative peak positions match well, and with the exception of the first and second peaks there is a good agreement in relative intensities.

3.4. Core holes

In order to account for the effect of the hole left when a core electron is excited in the electron energy loss process, a modified PAW data set can be used. These ‘core hole’ potentials are created for atoms with an empty (or fractionally-occupied) core orbital. Since these data sets result in a net charge being added to the simulation cell, care must be taken to converge results with respect to cell size due to the long range nature of the Coulomb force. Here linear-scaling DFT has particular strength as large cells, which might be infeasible with conventional plane wave codes, can be simulated.

As discussed in section 3.3, materials with wide band gaps only weakly screen the core hole charge. To achieve good agreement between simulated and experimental spectra in such materials, it is necessary to include the core hole [20]. For the wide band gap materials in section 3.1 a second set of simulations were conducted including a whole core hole in the $1s$ orbital.

In MgO the inclusion of a core hole is clearly beneficial in terms of improved agreement with experiment. The oxygen K edge shows a shift of peaks to higher energies relative to the first peak, correcting the peak energy underestimate seen in the non-core-hole spectrum and resulting in the impressive agreement seen in figure 3. Particularly encouraging results are seen for the magnesium K edge, where a significant increase in the intensity of the first peak relative to the second leads to a convincing match between theoretical and experimental spectra.

The remaining discrepancy between our predicted Mg K edge and the experimentally observed edge is due primarily to our choice of broadening scheme. We have elected to adopt a simple energy dependent Lorentzian broadening, which has the effect of reducing the intensity of peaks at higher energies relative to those at lower energies. As a result of this the relative intensity of the second and third peaks in the structure at 1320 eV is reversed.

In the case of diamond (figure 4) there is a change in the relative intensities of the first two peaks, which now show the correct intensity ordering with respect to experiment. Note also that, the spacing of the first and second peaks is increased from 5.37 eV to 6.35 eV, meaning that the position of the second peak with respect to the experimental spectrum

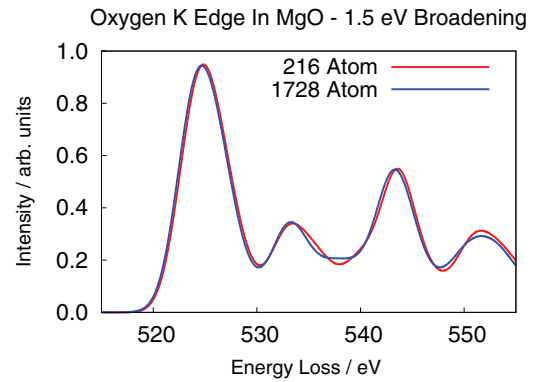


Figure 5. Size convergence of the oxygen K edge in MgO with respect to system size. With a Gaussian broadening of 1.5 eV there is only a modest difference in the two computed spectra. Examining the unbroadened spectra indicates that the improved accuracy of Γ point sampling in the 1728 atom cell is responsible for the difference.

(spacing around 6.1 eV) changes from being slightly underestimated to slightly overestimated.

For graphite, in figure 4, the increased screening effects reduce the impact of including a core hole on the computed spectrum. An improvement in the relative spacing of the π^* and σ^* peak onsets is seen, which when combined with energy dependent broadening (taking into account the short lifetime of excitations to high energy conduction band states) a very good agreement with experiment is expected.

3.5. Convergence with system size

The inclusion of a core hole raises the issue of convergence with respect to system size, as in insulating materials the Coulomb interaction between periodic images is very long ranged. To investigate how large a simulation cell would be needed to obtain a well converged spectrum the magnesium oxide system was selected. Starting with the 216 atom simulation cell of MgO used previously, we construct an eight fold replica of this simulation cell, containing 1728 atoms. A smaller 64 atom cell was also constructed and used with CASTEP with a $6 \times 6 \times 6$ k -point grid. We compute the oxygen K edge electron energy loss spectrum for the two larger cells and compute the Mizoguchi edge offset energy for all three.

Examining the Mizoguchi edge offset energies we see that there is a significant under convergence in the 64 atom cell with respect to the 216 atom cell. The computed energy for this system is 541.1 eV, differing by 485 meV from the offset computed for the 216 atom with Γ point sampling (540.6 eV). Going from the 216 atom cell to the 1728 atom cell we see that the former is close to converged, with a computed offset of 520.8 eV compared to 521.1 eV for the larger system (difference 240 meV). The computed spectra in figure 5 also confirm that the 216 atom system is well converged both with respect to electrostatics and k -point sampling. While the differences in computed edge offset energies may seem small we stress that when combining spectra of multiple atoms to produce a simulated spectrum of a sample of finite thickness these small differences could greatly alter the predicted peak

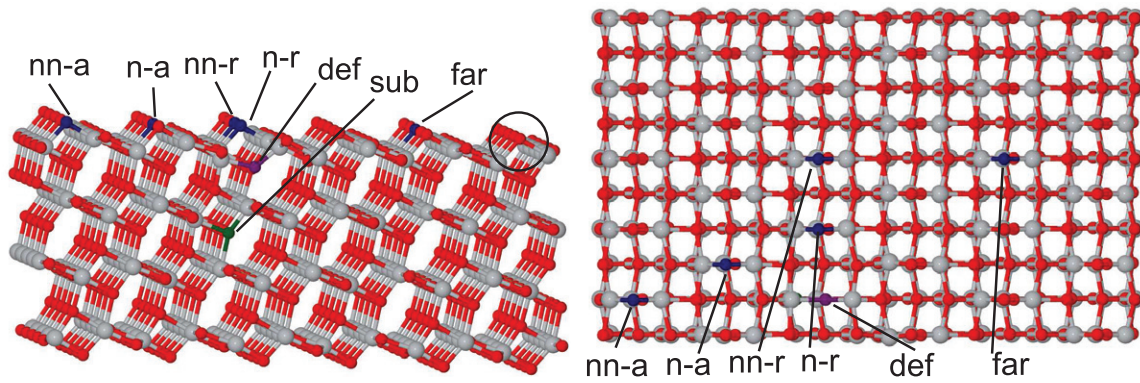


Figure 6. The defective cell studied. An atom equivalent to the one circled was deleted from a perfect surface model and the geometry of the cell optimized. Spectra were then computed for the six atoms indicated. From top left to bottom right these are second nearest neighbour in the row (nn-r), a far atom (far), nearest neighbour in row (n-r), the nearest neighbour across the rows (n-a), second nearest neighbour (nn-a) and the atom which was directly below the atom removed to form the defect (def) which is shown in purple. For computing the combined spectra shown in figure 9 the spectrum for a subsurface atom (sub) shown in dark green was also computed.

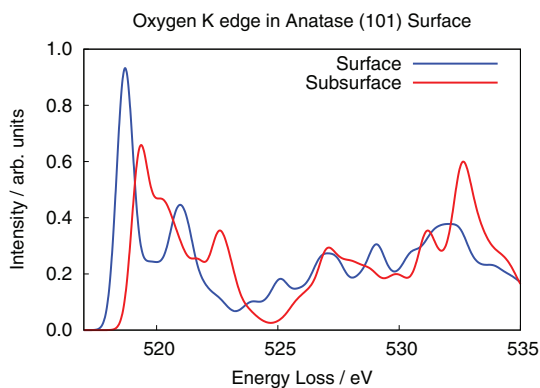


Figure 7. Predicted oxygen K edge spectra of surface and bulk atoms in a perfect anatase (1 0 1) slab. The differences between these spectra may be sufficient to resolve the surface signal experimentally using a method similar to that described in [6]. The subsurface atom used was one of those directly below a surface bridging oxygen: it occupied the same position as the ‘def’ atom did prior to relaxation.

widths in the resulting spectrum. We therefore propose that when performing calculations with the intent of combining spectra from multiple atoms it is necessary to use simulation cells containing on the order of at least two hundred atoms in order to correctly converge the offsets which must be applied to those spectra prior to their combination.

4. Anatase surfaces

Finally, we present a practical example of the use of the current methodology, namely to predict the influence of surfaces and defects on the EEL spectra of anatase. This system provides an excellent demonstration of the utility of ONETEP, since in order to fully relax defect geometries, very large cells are needed. This is particularly true for charged defects, which produce long-ranged electrostatic and strain fields.

First, we construct a 720 atom slab of pristine anatase with (1 0 1) surfaces exposed on both sides, surrounded by a 36 Å vacuum gap. The slab geometry was relaxed using the ONETEP implementation of the BFGS algorithm [39] so that all forces

Table 2. Distances to the relaxed defect atom of the atoms whose K edges were computed.

Atom	Distance to defect / Å
def	0.0
n-r	4.46
nn-r	8.01
n-a	6.36
nn-a	10.96
far	12.54
sub	4.00

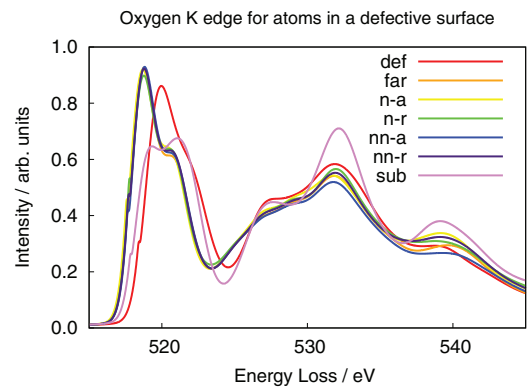


Figure 8. Predicted oxygen K edge spectra of the surface atoms in figure 6. Here we see that all atoms not directly adjacent to the defect produce very similar spectra. The spectrum produced by the atom closest to the defect (‘def’) produces a spectrum with a different shape and edge onset energy; these two features could be used to identify the presence of a defect. We show in figure 9 that these differences stand out even against a modest background signal for other atoms.

were below $0.1 \text{ eV } \text{Å}^{-1}$. We refer to this system as the ‘pristine’ slab.

A second surface cell was then prepared, containing a doubly positive oxygen vacancy formed by removal of one of the surface bridging oxygen atoms. The geometry of this cell was also relaxed, leading to the simulation cell shown in figure 6. We refer to this as the ‘defective’ system.

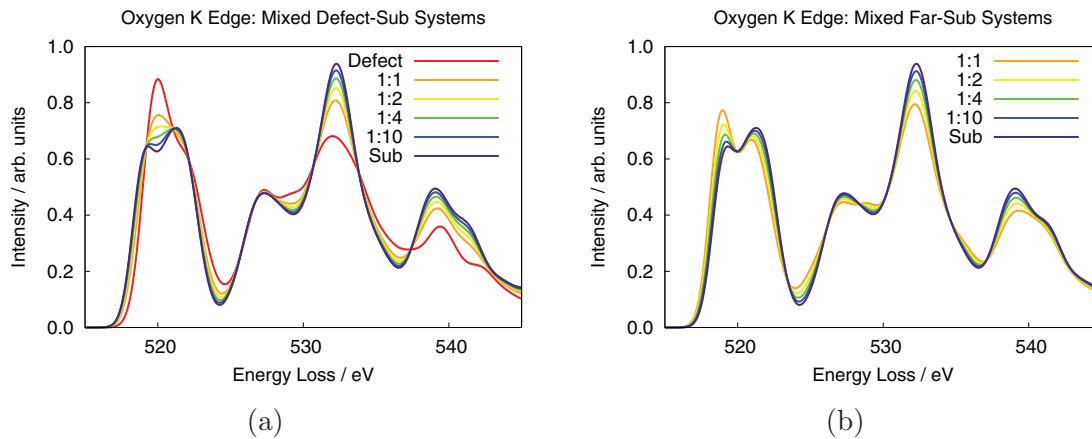


Figure 9. Predicted spectra for a defective surface with contributions from multiple atoms: oxygen K edge spectra for the sub surface atom combined with that for the defect atom (a) and far atom (b). The objective is to simulate taking a spectrum for a sample of finite thickness. The spectra shown in (b) are intended to represent those of pristine slabs of various thicknesses. It can be seen that only in a thin sample would the contribution of the defect be resolvable at realistic energy resolutions: a 0.7 eV Gaussian broadening is used here.

The oxygen K edge energy loss spectrum for a bridging surface oxygen atom for the pristine slab was computed and is shown in figure 7. In all cases, a whole core hole in the oxygen $1s$ orbital was used. One of the most recognizable features of the anatase oxygen K edge is reproduced, namely the double peak separated by 2.26 eV. The relative intensity of the two peaks differs somewhat from experimental spectra, where they have an approximate 1 : 1 ratio. This may be expected for under-coordinated surface bridging oxygen atoms, as a similar intensity ratio is seen in x-ray absorption spectra of anatase (1 0 1) surfaces [40]. Also shown in figure 7 is the spectrum for a sub-surface oxygen atom, this spectrum shows significant differences from the spectrum of the bridging atom: there is a reduction in intensity of the first peak relative to the second and an increase in peak separation. Together these changes should make it possible to resolve between surface and bulk spectra using a method like that in [6]. In [6] a series of electron energy loss spectra were taken through areas of a sample with differing thickness and therefore differing contributions of the bulk to the recorded spectrum. A principal components method was then used separate the surface contribution to the spectra.

Electron energy loss spectra were computed for a selection of six oxygen atoms at various distances from the defect in the defective system, as indicated in figure 6. Distances of these atoms to the defect are given in table 2.

For each position, the edge offset was calculated according to the method of Mizoguchi. The edge offset for the defective atom was found to be 518.9 eV and for the sub-surface atom was 518.7 eV. The other atoms have offsets of between 518.3 and 518.4 eV. These are measurable differences given sufficient energy resolution, but it is worth noting that the uncertainty in the calculated values due to convergence with respect to system size could be of similar or greater magnitude as described in section 3.5.

Examining figure 8, we see that the expectation that electron energy loss spectroscopy is sensitive only to short-ranged effects is clearly borne out for this system. The oxygen K edge for the atom far from the defect is effectively identical to an

equivalent atom in the pristine slab. We may conclude that a high concentration of defects must be present to significantly alter an spectrum which is averaged over a large area, as only atoms very close to a defect will produce contributions to the spectrum which differ from that of a pristine slab.

Although EELS is expected to be a surface-sensitive method, an electron beam nevertheless penetrates a certain distance into a slab. In a real experimental measurement for an anatase slab, even if the lateral resolution of a beam is very high, spectra from multiple atoms at different depths into the slab are likely to be mixed, leading to an averaged spectrum. In figure 9 we have simulated this mixing effect by taking a weighted combination of spectra for two atoms lying on a vertical line through the sample and thus likely to be excited by the same electron beam. The mixing ratios have been chosen to reflect slabs of varying thickness, with the 1 : 3 defect:sub-surface ratio approximating the slab depicted in figure 6. Figure 9 highlights the challenges faced in identifying a defect using EELS. We can see however that the structure of the first peak, at approximately 520 eV, changes considerably between the defect spectrum and that of atoms in the layers below. This change in structure is visible even with considerable broadening and thus there is some hope that in sufficiently thin samples the presence of intrinsic defects would be detectable.

5. Conclusions

We have demonstrated an efficient method for the computation of electron energy loss spectra for large, complex nano-materials systems. This approach has been implemented in the linear scaling code ONETEP. We have tested our method against both experimental spectra and other well-established simulation methods (both plane-wave and all-electron methods); plane wave and all-electron. We have also demonstrated successful implementation of core-hole and absolute energy shift calculations. In all cases convincing agreement is obtained, with core holes being required in the case of comparisons to experiment, particularly in wide band-gap materials.

This represents a robust test of both the matrix element generation method and the conduction optimisation method used by ONETEP which has not previously been extensively tested with bulk solid systems.

As ONETEP does not yet support spin-orbit coupling, we expect poor reproduction of edges where this effect is significant, such as $L_{2,3}$ edges of heavier elements. Our methodology is, however, readily adaptable to include spin-orbit coupling, which can be implemented relatively straightforwardly into the PAW framework, so we are confident that edges with significant splitting could also be reproduced in principle.

The convergence of predicted spectra with respect to system size in large band gap materials was investigated using the prototypical insulating system magnesium oxide. We found that for the purposes of comparison to experiment, simulations are well converged within supercells of manageable size, namely in the region of 200–1000 atoms.

As an application of our method to a system of high technological relevance, we investigated the (1 0 1) surface of anatase, and the impact of defects on the spectra of that surface. We have confirmed that since the electron energy loss technique is very local, surface point defects are likely to only be identifiable in thin specimens, in experiments with atomic resolution. However, extended defects such as the columns of atoms in a grain boundary, which have different coordination number from their bulk counterparts, should be readily distinguishable with the current tools.

Acknowledgments

This work was performed using the Darwin Supercomputer of the University of Cambridge High Performance Computing Service (www.hpc.cam.ac.uk/), provided by Dell Inc. using Strategic Research Infrastructure Funding from the Higher Education Funding Council for England and funding from the Science and Technology Facilities Council. EWT was supported by the EPSRC Cambridge NanoDTC, EP/G037221/1. LER was supported, in part, by DOE Office of Science User Facility under Contract DE-AC02-06CH11357. NDMH Acknowledges the support of the Winton Programme for the Physics of Sustainability. ONETEP development is supported by EPSRC platform grant EP/J015059/1. We wish to acknowledge the use of the EPSRC's Chemical Database Service at Daresbury. The authors thank Dr Caterina Ducati for useful discussions. The underlying data of this publication can be accessed via the following persistent URI: www.repository.cam.ac.uk/handle/1810/253717

References

- [1] Han W Q, Wu L, Zhu Y, Watanabe K and Taniguchi T 2008 *Appl. Phys. Lett.* **93** 223103
- [2] Takigawa Y, Ikuhara Y and Sakuma T 1999 *J. Mater. Sci.* **34** 1991–7
- [3] Tizei L H G, Nakanishi R, Kitaura R, Shinohara H and Suenaga K 2015 *Phys. Rev. Lett.* **114** 197602–7
- [4] Nicholls R J, Ni N, Lozano-Perez S, London A, McComb D W, Nellist P D, Grovenor C R, Pickard C J and Yates J R 2015 *Adv. Eng. Mater.* **17** 211–5
- [5] Ramasse Q M, Seabourne C R, Kepaptsoglou D M, Zan R, Bangert U and Scott A J 2013 *Nano Lett.* **13** 4989–95
- [6] Zhu G Z and Botton G A 2014 *Microsc. Microanal.* **20** 649–57
- [7] Goode A, Hine N, Chen S, Bergin S, Shaffer M, Ryan M, Haynes P, Porter A and McComb D 2014 *Chem. Commun.* **50** 6744–7
- [8] Skylaris C K, Haynes P D, Mostofi A A and Payne M C 2005 *J. Chem. Phys.* **122** 084119
- [9] Wilkinson K A, Hine N D M and Skylaris C K 2014 *J. Chem. Theory Comput.* **10** 4782–94
- [10] Hohenberg P and Kohn W 1964 *Phys. Rev.* **136** B864
- [11] Kohn W and Sham L J 1965 *Phys. Rev.* **140** A1133–8
- [12] Hernández E, Gillan M J and Goringe C M 1996 *Phys. Rev. B* **53** 7147–57
- [13] Skylaris C K, Mostofi A A, Haynes P D, Diéguez O and Payne M C 2002 *Phys. Rev. B* **66** 035119
- [14] Kohn W 1996 *Phys. Rev. Lett.* **76** 3168–71
- [15] Baer R and Head-Gordon M 1997 *Phys. Rev. Lett.* **79** 3962–5
- [16] Skylaris C K and Haynes P D 2007 *J. Chem. Phys.* **127** 164712
- [17] Ratcliff L E, Hine N D M and Haynes P D 2011 *Phys. Rev. B* **84** 165131–41
- [18] Blöchl P E 1994 *Phys. Rev. B* **50** 17953–79
- [19] Hine N D M 2016 Linear-scaling plane-wave density functional theory using the projector augmented wave method In preparation
- [20] Gao S P, Pickard C J, Payne M C, Zhu J and Yuan J 2008 *Phys. Rev. B* **77** 115122
- [21] Nicholls R J, Morris A J, Pickard C J and Yates J R 2012 *J. Phys.: Conf. Ser.* **371** 12–62
- [22] Mizoguchi T, Tanaka I, Gao S P and Pickard C J 2009 *J. Phys.: Condens. Matter* **21** 104204
- [23] Trucano P and Chen R 1975 *Nature* **258** 136–7
- [24] Lian C S, Wang X Q and Wang J T 2013 *J. Chem. Phys.* **138** 024702
- [25] Többsen D, Stüßer N, Knorr K, Mayer H and Lampert G 2001 E9: the new high-resolution neutron powder diffractometer at the berlin neutron scattering center *Mater. Sci. Forum* **378** 288–93
- [26] Bernuy-Lopez C, Allix M, Bridges C A, Claridge J B and Rosseinsky M J 2007 *Chem. Mater.* **19** 1035–43
- [27] Fletcher D A, McMeeking R F and Parkin D 1996 *J. Chem. Inf. Comput. Sci.* **36** 746–9
- [28] Mizoguchi T, Matsunaga K, Tochigi E and Ikuhara Y 2012 *Micron* **43** 37–42 (applications of EELS in materials and physics research)
- [29] Mizoguchi T, Tanaka I, Yoshioka S, Kunisu M, Yamamoto T and Ching W Y 2004 *Phys. Rev. B* **70** 045103
- [30] Mizoguchi T, Varela M, Buban J P, Yamamoto T and Ikuhara Y 2008 *Phys. Rev. B* **77** 024504
- [31] Tanaka I, Mizoguchi T and Yamamoto T 2005 *J. Am. Ceram. Soc.* **88** 2013–29
- [32] Clark S J, Segall M D, Pickard C J, Hasnip P J, Probert M J, Refson K and Payne M 2005 *Z. Kristall.* **220** 567–70
- [33] Adamo C and Barone V 1999 *J. Chem. Phys.* **110** 6158–70
- [34] Jollet F, Torrent M and Holzwarth N 2014 *Comput. Phys. Commun.* **185** 1246–54
- [35] Lejaeghere K, Speybroeck V V, Oost G V and Cottenier S 2014 *Crit. Rev. Solid State Mater. Sci.* **39** 1–24
- [36] ELK project <http://elk.sourceforge.net> (accessed: 20th February 2016)
- [37] Lindner T, Sauer H, Engel W and Kambe K 1986 *Phys. Rev. B* **33** 22–4
- [38] Hamon A L, Verbeeck J, Schryvers D, Benedikt J and Van der Sanden R M C M 2004 *J. Mater. Chem.* **14** 2030–5
- [39] Hine N D M, Robinson M, Haynes P D, Skylaris C K, Payne M C and Mostofi A A 2011 *Phys. Rev. B* **83** 195102
- [40] Thomas A G *et al* 2007 *Phys. Rev. B* **75** 035105